https://doi.org/10.5194/amt-2022-159
Preprint. Discussion started: 10 June 2022

Atmospheric Measurement Techniques
Discussions

Phase correlation on the edge for estimating cloud motion

Bhupendra A. Raut[1,2], Scott Collis[1,2], Nicola Ferrier[1,2], Paytsar Muradyan[2], Rajesh Sankaran[1,2], Robert Jackson[1,2], Sean Shahkarami[2,3], Seongha Park[1,2], Dario Dematties[1,2], Yongho Kim[1,2], Joseph Swantek[1,2], Neal Conrad[1,2], Wolfgang Gerlach[1,2], Sergey Shemyakin[2,3], and Pete Beckman[1,2]

[1]Northwestern-Argonne Institute of Science and Engineering, Northwestern University, Evanston, Illinois, USA.
[2]Argonne National Laboratory, Lemont, Illinois, USA.
[3]University of Chicago, Chicago, Illinois, USA

Correspondence: Bhupendra Raut (braut@anl.gov)

Abstract. Phase Correlation (PC) is a well-known method for estimating cloud motion vectors (CMV) from infrared and visible spectrum images. Commonly phase-shift is computed in the small blocks of the images using the fast Fourier transform. In this study, we investigate the performance and the stability of the block-wise PC method by changing the block size, the frame interval, and combinations of red, green, and blue (RGB) channels from the total sky imager (TSI) at the United States Atmospheric Radiation Measurement user facility's Southern Great Plains site. We find that shorter frame intervals, followed by larger block sizes, are responsible for stable estimates of the CMV as suggested by the higher autocorrelations. The choice of RGB channels has a limited effect on the quality of CMV, and the red and the grayscale images are marginally more reliable than the other combinations during rapidly evolving low-level clouds. The stability of CMV was tested at different image resolutions with an implementation of the optimized algorithm on the Sage cyberinfrastructure testbed. We find that doubling the frame rate outperforms quadrupling the image resolution in achieving CMV stability. The correlations of CMV with the wind data are significant in the range of 0.38–0.59 with a 95% confidence interval, despite the uncertainties and limitations of both datasets. The raindrop contaminated images were excluded by identifying the rotation of the raindrop contaminated TSI mirror in the motion field. The results of this study are critical to optimizing algorithms for edge-computing enabled sensor systems.

1 Introduction

Converting cloud images captured by a ground-based sky-facing camera into a time series of motion vectors has implications for reporting local weather and short-term forecasting of solar irradiance (Jiang et al., 2020). Phase Correlation (PC) estimates translative shift between two similar images by detecting a peak in their cross-correlation matrix which is used to estimate the cloud motion vectors (CMV) from the satellite and ground-based sky camera images (Leese et al., 1971; Dissawa et al., 2017; Zhen et al., 2019). Other object-based cloud tracking methods used in radar and satellite meteorology require cloud identification before the tracking stage. The cloud identification approaches vary from threshold-based to texture-based methods and machine learning methods (Steiner et al., 1995; Raut et al., 2008; Park et al., 2021).

https://doi.org/10.5194/amt-2022-159
Preprint. Discussion started: 10 June 2022

The texture-based methods and the machine learning models add computational overhead complicating their use in real-time applications. In infrared and microwave satellite images, and radar images, the threshold of brightness temperatures and reflectivity, mark a physical distinction of the features in the scene. However, for the cloud images in the visible spectrum, thresholds of RGB values may not be a meaningful criterion to distinguish the properties of the clouds because they are affected by the lighting conditions and time of the day. The texture-based techniques are also susceptible to detection errors due to reflections and shadows caused by solar zenith angle. While the optical flow method can also estimate dense field motion, it also suffers from the limitations in visible camera images and requires segmentation or background subtraction before the images are processed (Denman et al., 2009; Wood-Bradley et al., 2012; El Jaouhari et al., 2015).

The Sage Project is designing and building a new kind of reusable cyberinfrastructure composed of geographically distributed sensor systems (sage nodes) that include cameras, microphones, and weather and air quality sensors generating large volumes of data that are efficiently analyzed by an embedded computer connected directly to the sensor at the network edge (Beckman et al., 2016, https://sagecontinuum.org/). An edge device rapidly analyzes the data in real-time at the location where it is collected, and continuously sends and receives feedback from connected remote computing systems and other similar devices. In such networks including Sage, the computational efficiency of the algorithm is critical. The PC method can be implemented without preprocessing images and is robust to noise and changes in illumination as it works by only correlating the phase information (Chalasinska-Macukow et al., 1993; Turon et al., 1997). This eliminates the burden of separating the background from the objects to be tracked. A straightforward implementation of the PC method in the frequency domain using the fast Fourier transform (FFT) is computationally efficient, and hence a natural choice to detect the cloud motion vectors from the hemispheric camera images at the edge.

The PC method is efficient for uniform rigid body motion, i.e. when an object's shape and size are preserved, and multiple objects in the scene are moving with the same velocity. There are a few limitations to the PC method that can affect the applicability of using it to track cloud motions in a sky-facing camera. First, the PC method is less efficient when multiple peaks in the correlation matrix are observed. This occurs when cloud features are moving with different velocities as each peak is associated with the motion of one or more independent features in the images. This limitation is overcome by dividing the image into sufficiently smaller subregions or blocks and employing the PC separately for each block (Leese et al., 1971).

Second, the changing cloud texture and geometries may cause incoherent motion vectors in some image blocks. Therefore, additional quality control measures are applied to remove the spurious CMVs, usually assuming that a spurious CMV substantially deviates from its surrounding CMVs in the presumably smooth velocity field (Westerweel and Scarano, 2005). For the assumption of the coherent velocity field, smaller block sizes are preferred. The optimal block size is determined by the maximum expected displacement during the frame interval.

Third, the ground-based cameras frequently encounter contamination on the mirror dome or hemispherical lens, obscuring the clouds during and after a precipitation event and automated identification and removal of precipitation-contaminated images are critical (Heinle et al., 2010; Kazantzidis et al., 2012; Gacal et al., 2018; Voronych et al., 2019). The distortion of images caused by the presence of raindrops and the edge detection methods are used to identify raindrop contamination (Kazantzidis et al., 2012; Voronych et al., 2019). In this paper, we propose the use of motion vectors for detecting raindrop contamination on the rotating TSI mirror.

Finally, while it is common for cameras to produce high-resolution three-channel images, the PC method utilized only a single channel. Hence, either the grayscale image or one of the RGB channels is used. The dependence of CMV stability on the choice of image channels is undocumented.

Investigating the sensitivity of the motion vectors to the block sizes, the frame frequency, and its response to different spectral channels will help in the effective implementation of the method. Therefore, in this paper, we evaluate the performance of the block-wise PC with three visible channels, the grayscale, and the red to the blue ratio in two blocksizes and two frame rates. We also demonstrate the effect of change in the image resolution and the change in frame rate on the CMV quality. The data, methodology and the algorithm are described in section 2. The results are shown in section 3, and their implications for the Sage edge-computing platform are discussed in section 4.

2 Data and Methods

2.1 Data

In this paper, we mainly used data from the Atmospheric Radiation Measurement (ARM) user facility's Southern Great Plains (SGP) atmospheric observatory (36.7°N, 97.5°W), in particular, at the supplemental S1 and central C1 facilities in Lamont, OK, due to long-term data availability from colocated instruments for wind and cloud base height measurements. The Sage camera images are used in section 3.2.2.

2.1.1 Total Sky Imager

The Total Sky Imager (TSI) is a mounted full-color digital camera looking downward toward a rotating hemispherical mirror. Daytime full-color hemispheric sky images are obtained from TSIs operational at the ARM SGP atmospheric observatory (Morris, 2005; Slater et al., 2001). The images recorded over the S1 site every 30 seconds (Morris, 2000) during the day on July 26, 2016, are used to demonstrate the sensitivity of the method described later on. The central sky region of 400×400 pixels is used to compute the CMV during the 06:36 to 20:35 CDT window. The data over the C1 site are used for comparison of CMVs with the wind data.

2.1.2 Sage Camera

Hanwha Techwin America's fish-eye camera (XNF-8010RV X series), hosted on the atop a Sage node and pointed toward the sky at the Argonne Testbed for Multiscale Observational Studies (ATMOS) (41.70°N, 87.99°W), has a 6 MP CMOS sensor providing 2048×2048 pixels full-color images. Unlike the TSI camera, the Sage fish-eye camera lacks a sunband and a rotating mirror. Images recorded from this camera every 30 seconds from 06:00 to 17:00 CDT on February 13 and 14, 2022, are used to demonstrate the effect of camera resolution and frame rate on the sensitivity of the method.

2.1.3 WPR and CEIL

To validate the estimates of the CMV in our work, measurements from the co-located ceilometer and the wind profiling radar (WPR) (Muradyan and Coulter, 1998; Morris et al., 1996) were used from the SGP C1 site from October 14, 2017, to August 14, 2019. We used the cloud base height (CBH) estimates for the same period from the laser ceilometer, with its measurements extending up to 7.7 km in 10 m resolution. The ceilometer is an autonomous, ground-based active remote sensing instrument, that transmits near-infrared pulses of light and detects multi-layer clouds from the signal backscattered from cloud droplets that reflect a portion of the energy back toward the ground. (Morris, 2016). The wind profiles for comparison were obtained from the 915 MHz WPR, which transmits electromagnetic pulses in vertical and multiple tilted directions (3-beam configuration is used at SGP) to measure the Doppler shift of the returned signal due to atmospheric turbulence from all heights (Muradyan and Coulter, 2020). The consensus-averaged winds are estimated at an hourly interval and are available from 0.36 km to about 4 km at 60 m vertical resolution.

2.2 Phase Correlation using FFT

The PC in each image block, between the subsequent images, is computed using FFT (Leese et al., 1971). The following procedure is used to estimate the shift in images $I_1(i,j)$ at time $t1$ and $I_2(i,j)$ at time $t2$:

1. Obtain FFT of the images $I_1(i,j)$ and $I_2(i,j)$ as $I_1(\mu,\nu)$ and $I_2(\mu,\nu)$.
2. Compute $C(\mu,\nu)$ by multiplying FFT of the first image and complex conjugate of the second image.
3. Obtain an inverse FFT of $C(\mu,\nu)/|C(\mu,\nu)|$

The real part of the outcome gives covariance matrix $Cov(p,q)$. An example of the procedure is given in Raut et al. (2021).

Sharp single-pixel peaks can occur in the correlation matrix, due to the high-frequency noise and artifacts in the images, which are flattened using Gaussian smoothing on Cov(p,q) with $\sigma = 3$. The location of the peak covariance gives the shift in the images.

2.3 Outliers in the CMV Field

When the image block belongs to the clear sky or the scene has changed beyond recognition by the correlation, the peak in the covariance matrix is usually near the boundaries of the block, thus giving artificially large displacements. Such vectors are easily identified using a maximum velocity limit V_{max}. For this analysis, we used $V_{max} = \frac{block\ length}{3}$. If the V_{max} is smaller than the expected maximum speed, then a larger block size is recommended.

Removing large magnitude vectors smooths the field, however some motion vectors of reasonable magnitude but spurious directions remain. Such spurious vectors can be removed by comparing them with the surrounding motion vectors. We compared each vector with the normalized median fluctuation of the neighboring blocks as described in Westerweel and Scarano (2005) and Huang et al. (2011). The CMV vectors with normalized median fluctuation values over 6 are discarded.

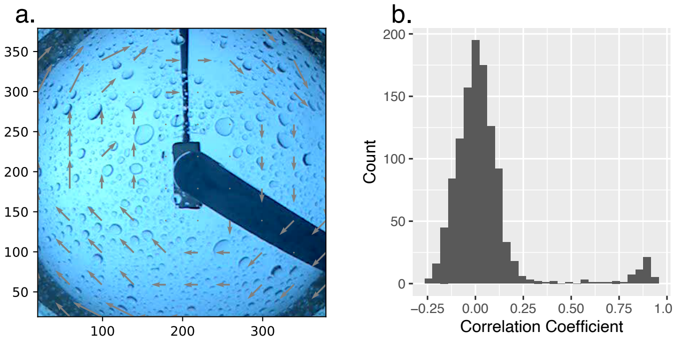

Figure 1. a) An example of the circular motion field generated every 2-4 minutes by rotation of the raindrop contaminated mirror of TSI. b) Histogram of the correlation coefficient between the mean rotational vector field and CMV fields on January 2, 2017 shows robust separation of raindrop contaminated frames from the clean frames.

2.4 Identification of Raindrop Contamination

The CMV is not valid when rainwater present on the reflecting mirror obscures the clouds. However, in such a scenario, the rotation of the raindrop contaminated mirror produces a rotating vector field as shown in Fig. 1a. We correlated the estimated CMV fields with the mean of manually identified contaminated CMV fields and found that the correlation coefficient, $r > 0.4$ is associated with the rotation of the raindrop contaminated mirror (Fig. 1b). Because of the sharp edges of the raindrops, the rotational pattern is efficiently captured with few raindrops contaminating the mirror. However, it struggles to detect contamination when the drops are concentrated at the center of the dome. Therefore, after the rotation is detected, the next 10 minutes of data are flagged as contaminated even if no subsequent rotation is detected.

2.5 Setup for Sensitivity Analysis

To test the algorithm's sensitivity to the block size, we divided the 400 × 400-pixel sky area into a grid of 10 × 10 and 20 × 20 blocks and referred to as block length 40 and 20 pixels, respectively in Figures 3–6. Note that the choices for the number or size of blocks are restricted by the V_{max} on one end and the neighborhood criteria on the other. For example, if the expected V_{max} is 7 pixels/min then the blocks should be at least 21 pixels wide (section 2.3). On the other hand, for the 10 × 10 grid (block width 40 pixels) with one pixel neighborhood, the correction applies to the central region of 8 × 8 blocks only. Therefore, increasing block sizes reduces the number of blocks in the sky region, which reduces the scope for the neighborhood method in the error correction stage. To test the sensitivity to the frame interval, CMVs are also computed at 30 and 60-second intervals. The 30-second CMVs are accumulated over one minute for comparison. As the PC uses monochromatic images, the CMVs were computed separately for the three BGR channels (abbreviated to Bu, Gn, Rd in Figures), the red to the blue ratio (RB, Slater et al., 2001), and grayscale (Gy) images.

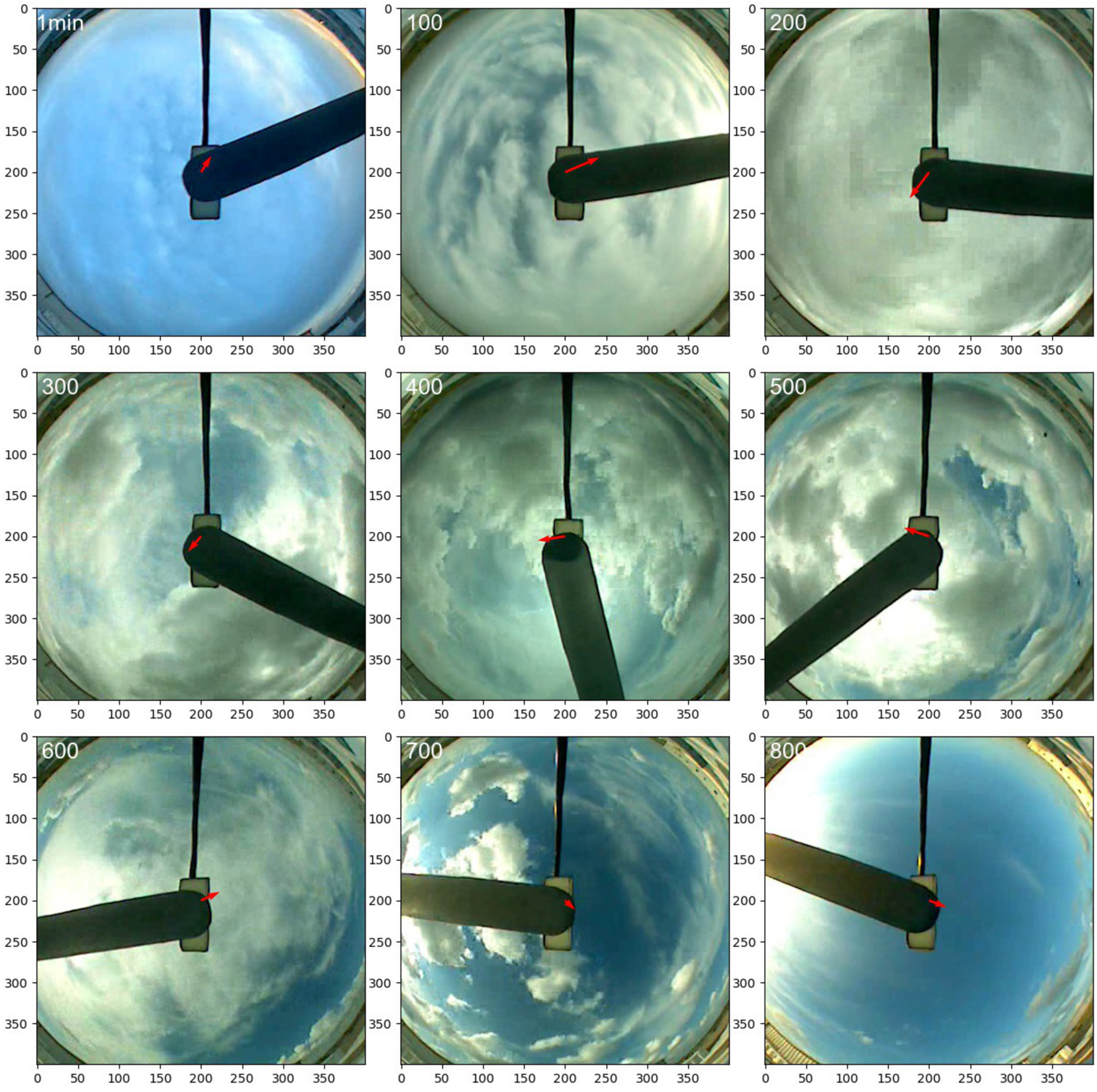

Figure 2. Varying sky conditions on 26 July 2016, during 06:36 to 20:35 CDT (11:36-01:35 next day in UTC) at 100 minutes interval over Lamont, OK. Sky area of 400x400 pixels is cropped and used for CMV computation. The top of the images point to the north and the red arrow shows direction of motion for that frame.

3 Results

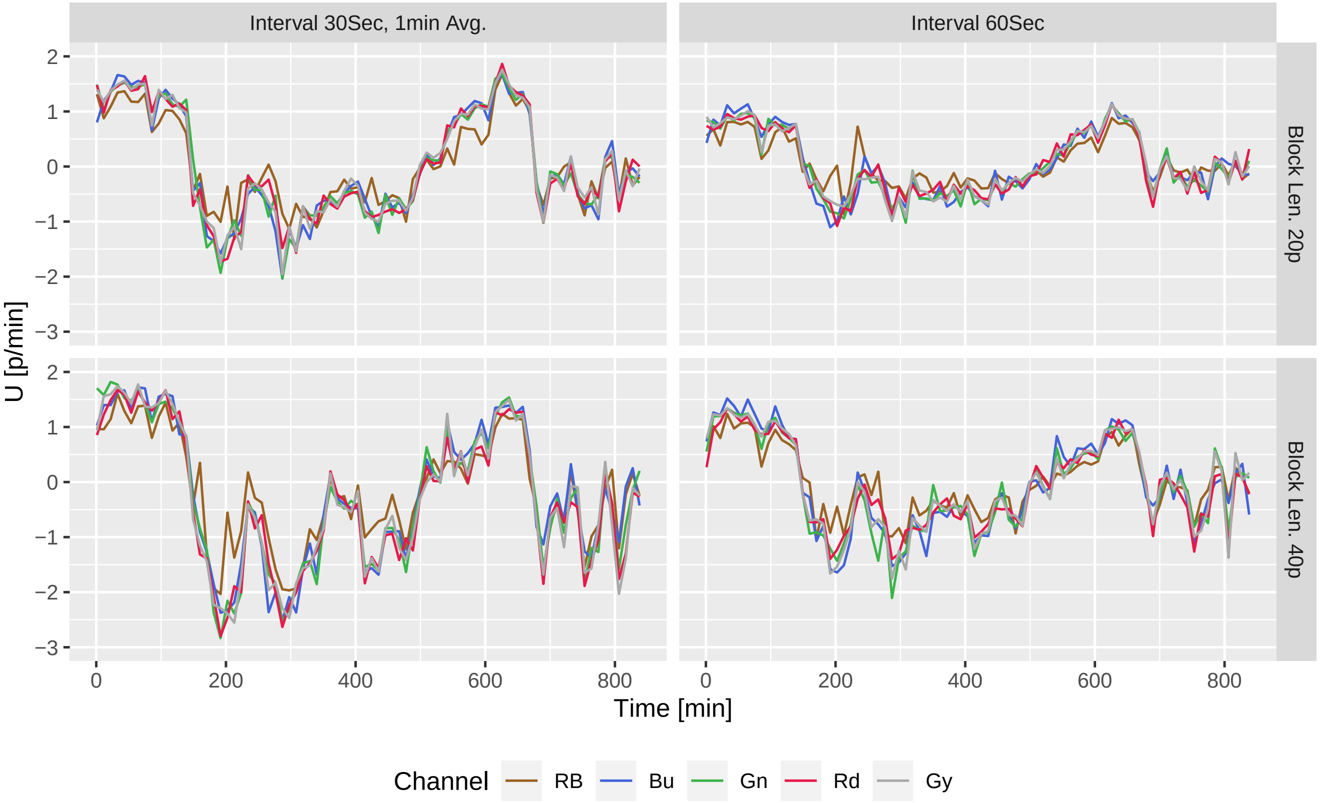

Figure 3. Smoothed time series of U component of domain averaged CMV [$\mathrm{pixel}\cdot\mathrm{min}^{-1}$] on 26 July 2016, 06:36 to 20:35 CDT (11:36-01:35 next day in UTC) over Lamont, OK. Variation with block size (20 pixels and 40 pixels) and frame intervals (30 sec and 60 sec) are shown for 5 channels.

3.1 Cloud Motion and Sensitivity Results

Changing sky conditions captured by TSI on July 26, 2016, during the 06:36 to 20:35 CDT are shown in Fig. 2 at 100 minutes intervals for reference. The sequence of images shows the movement of stratiform clouds from the southwest for over two hours (∼ 150 min), with the occasional presence of low-level cumulus clouds. After about 3 hours, the cumulus cloud development covered the sky (see the 200-minute snapshot) moving predominantly from the east/northeast, as shown by the red arrow. Rapidly moving low-level clouds had less coherent motion at the block level than the altostratus. In addition, the low-level clouds intermittently traveled in patches with the altostratus aloft moving from the southwest. The time series of U and V components of CMV, shown in Fig. 3 and Fig. 4, respectively, are smoothed using cubic splines for easily discernible visualizations. The raw output is shown in Fig. A1 and A2. The U and V plots suggest that the PC method successfully captured the direction of the motion and the reversal of the direction in all configurations. As described above, the mid-level clouds moving from the west and transition to low-level clouds moving from the east at around 150 minutes are seen in Fig. 3.

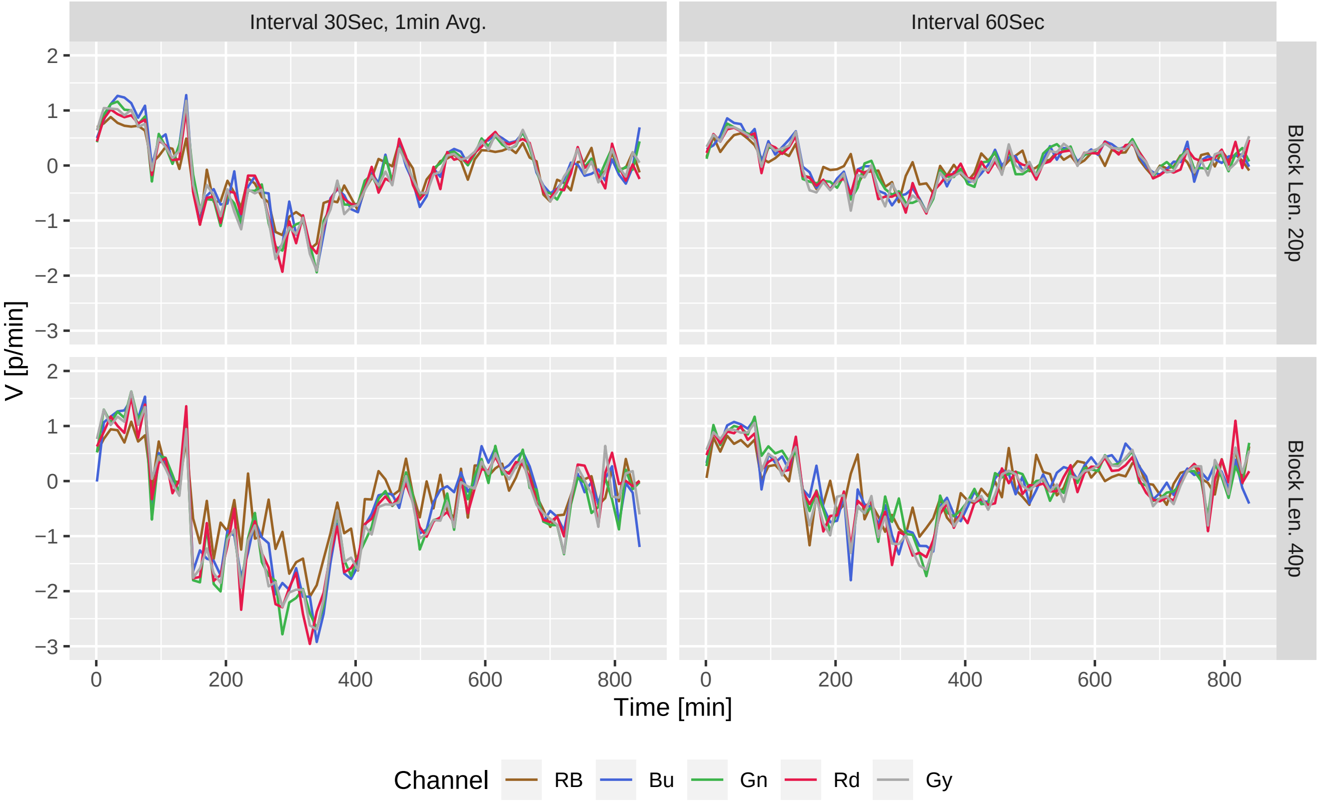

Figure 4. Same as Figure 3 but for V component of the CMV.

The turbulent motion characterized the episodes of cumulus growth from 150 to 450 minutes, as evidenced by the fluctuations in the CMV during this phase in all channels, however, more pronounced in the RB channel. Between 500 and 600 minutes, cumulus and altostratus cleared, and high-level cirrus clouds became visible, flowing from the west. Additional late-afternoon cumulus movement (see the 700 min snapshot) and the clear sky with high-level cirrus or occasional westward-moving low-level cloud patches were present until sunset.

The frequency distribution of the CMV components (Fig. 5) also shows two peaks of positive eastward component (U) distinguishing the rapidly moving mid-level and slow high-level clouds from the camera viewpoint. The larger blocks (40 pixels wide) and the shorter frame interval (30-sec) have a wider range than the rest of the configuration, which shows their efficiency at capturing the low-level cumulus motion. It is important to note that July 26, 2016, was accompanied by a variety of cloud conditions and individual episodes of the low, medium, and high-level cloud motion, each lasting for at least an hour. Thus, the short-term fluctuations of CMV are mainly caused by the algorithm's instability. To assess the stability of CMVs for various configurations, we compare the autocorrelation of the CMV in the following subsection.

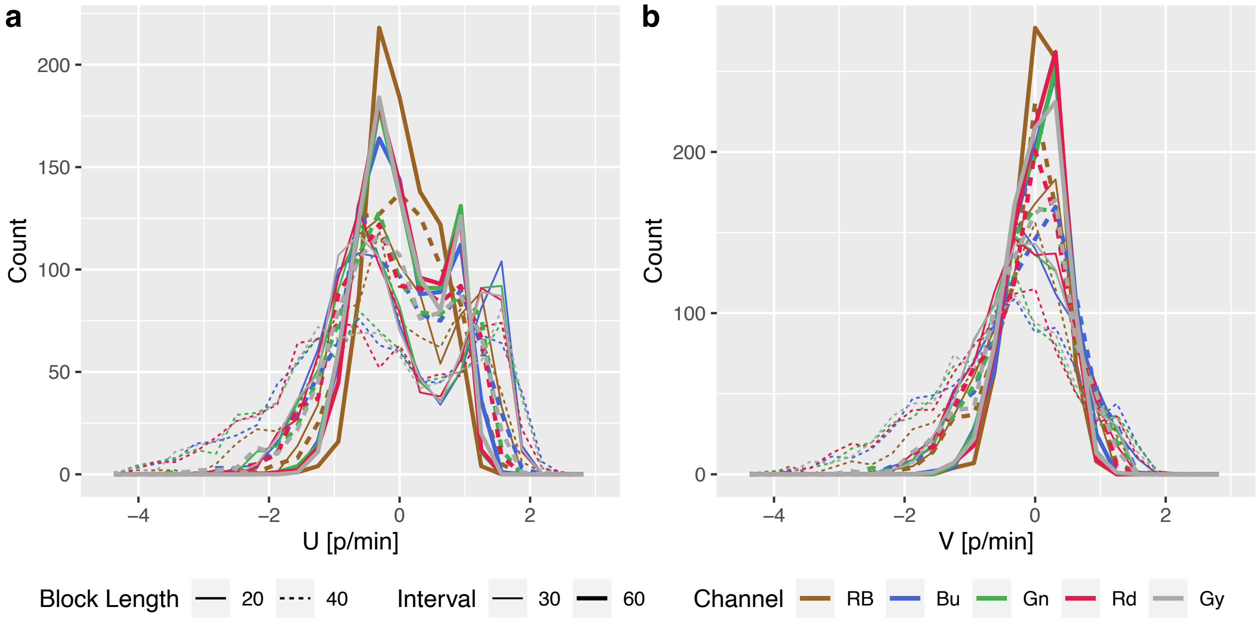

Figure 5. Frequency distributions of U and V components [pixel · min^{-1}] shown in Figures 3 and 4, respectively for all 20 setup combinations. The bimodal distribution of U component is due to two cloud regimes discussed in sec

3.1

3.2 Stability of CMV

The stability of the CMV was tested by changing the block size, the frame interval, and combinations of red, green, and blue (RGB) channels from the total sky imager (TSI) and by changing the image resolution and frame rate in the Sage camera.

3.2.1 Block Size, Frame Interval and Channel

The movement of clouds is usually smooth at the one-minute time interval. Except for the change in direction during the altostratus to cumulus transition, the movement of the clouds on July 26, 2016, should be more or less stable at the hourly intervals for most of the day (Fig. 3 and 4). However, the CMV fluctuates at a 1-minute time interval, mainly due to the irregular response of the algorithm caused by the issues mentioned in Section 1. Therefore, the stability of motion vectors in time is evaluated for the above configurations by checking the autocorrelation of the CMV time series. The autocorrelation function (ACF) of U and V components for different configurations is shown in Fig. 6 (top panels). The linear ACF suggests a long decorrelation length for all the combinations. While RB has the lowest autocorrelations (more fluctuating vectors) for all configurations, the rest of the color channels have more or less equally stable vectors. The frame interval, followed by block length, noticeably affects the stability of the vectors.

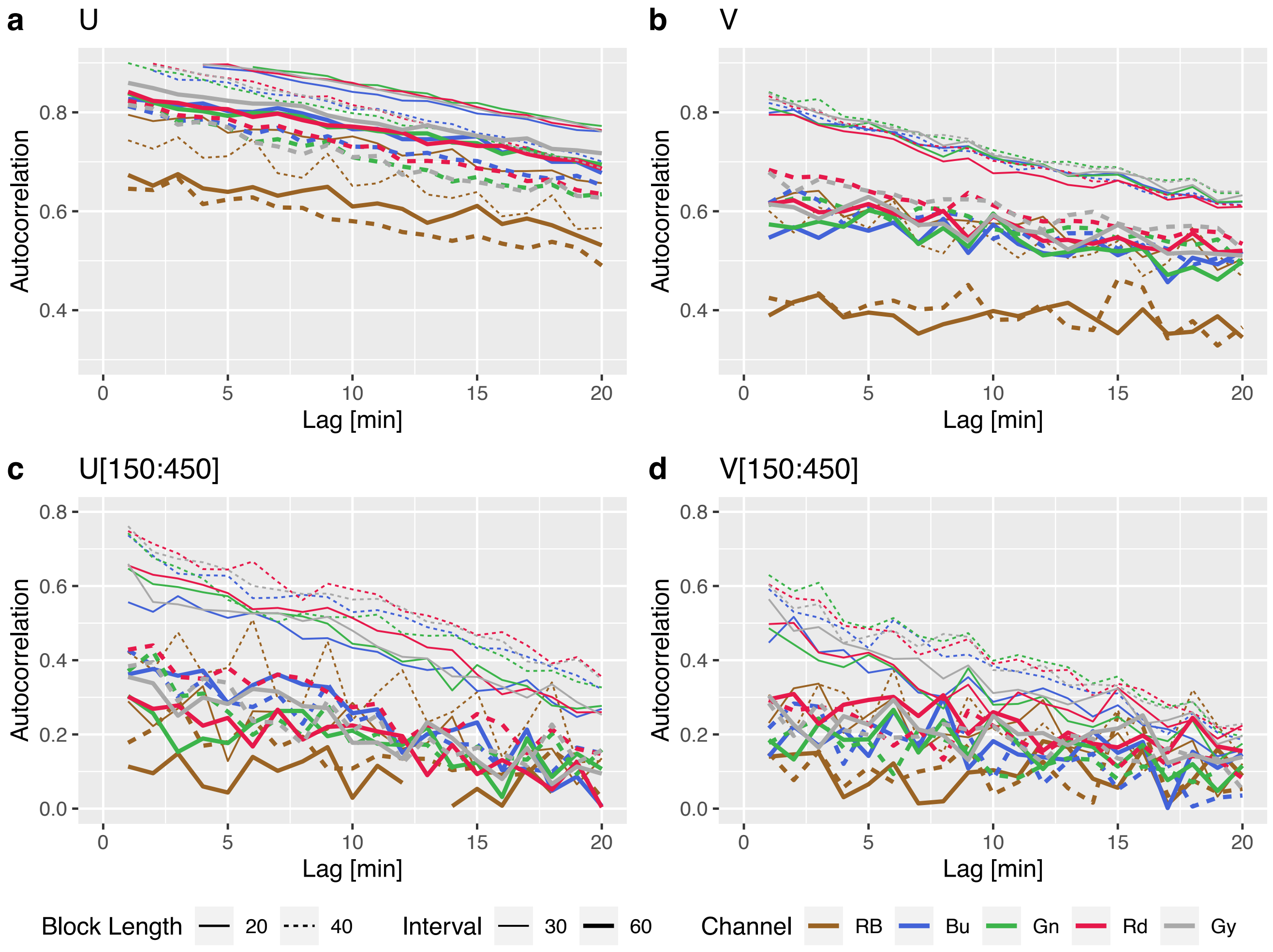

Figure 6. Autocorrelogram for U and V components showing the stability of the motion vectors shown in Figure 3 and Figure 4. (top) for all the data, and (bottom) for the selected period of rapid Cu cloud development between 09:06 to 14:56 LT (time steps: 150–500 in).

The lower panels in Fig. 6 are the same as the top panels but for the period between 150:450 minutes when the rapidly developing low-level clouds were present. The small cloud features were developing fast and had variable motion. Therefore, 175 during this period, the autocorrelation is lower and the performance of the large block sizes and short frame intervals is noticeably better for both U and V components. The CMV from red and gray channels has slightly higher autocorrelation for the dominant motion (i.e. zonal component, U) during this period.

3.2.2 Image Resolution and Frame Interval

Our analysis shows that CMVs are more stable for larger blocks and shorter frame intervals (see Sec. 3.2.1). Therefore, the 180 stability of motion vectors is evaluated for the same blocks (i.e., the image divided into 10×10 grid.) and by reducing their

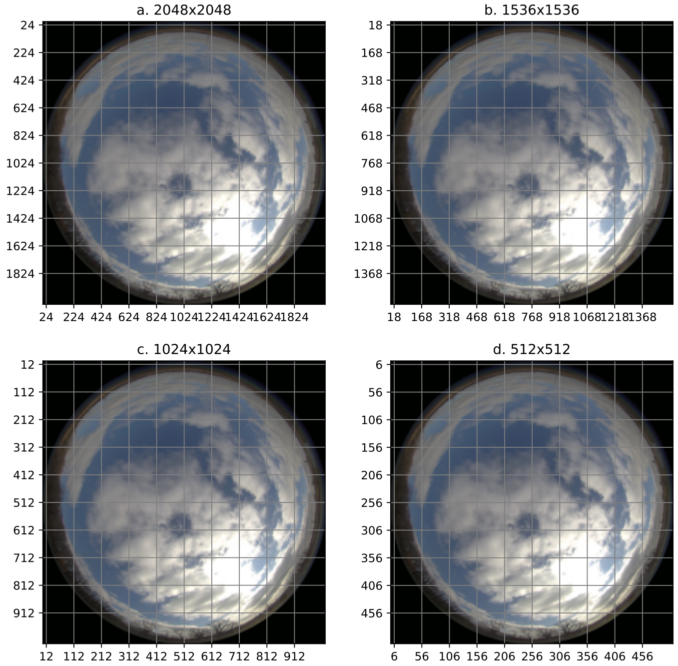

Figure 7. The scheme for testing resolution sensitivity with Sage camera image obtained on April 21, 14:06:38 over Lamont, OK. A 10×10 block grid with four successively lower resolutions is used for CMV computation to compare the effect of resolution and time interval on the stability of CMV.

resolution in steps to block lengths of 200, 150, 100, and 50 pixels, as shown in Fig. 7, with frame intervals of 30 and 60 seconds. February 13 was dominated by mid-level stratus cloud motion and February 14 had periods of low-level cumuliform development with fast movements and rapid evolution of cloud features dominating the scene. In addition, on both days, the cloud motion was mostly in East-West (zonal) direction with the U component approximately four times larger than the V component. Therefore, ACF of only U components for four image resolutions and two frame intervals are shown in Fig. 8. ACF is significantly lower for longer frame intervals. For example, long intervals reduce the autocorrelation at lag-1 from 0.75 at 30-sec interval to 0.5 at 60-sec interval (Fig. 8 a). This effect is even more prominent for the rapidly evolving cumuliform clouds (Fig. 8 b) where the autocorrelation at the lag-1 drops from 0.65 to 0.2. On the other hand, change in the resolution by a factor of four has minimal effect and change in lag-1 autocorrelation is within 0.05.

3.3 Comparison with Wind Data

The comparison of the CMV either from a ground-based camera or satellite deployed sensors with that of atmospheric winds, has several sources of uncertainty. The estimation and comparison of CBH and winds from the ceilometer and the wind profiler respectively, show sampling uncertainty. In addition, the cloud displacement from the camera viewpoint differs with altitude, and deeper convective clouds do not always move parallel to the low level winds. Therefore, this comparison may not be

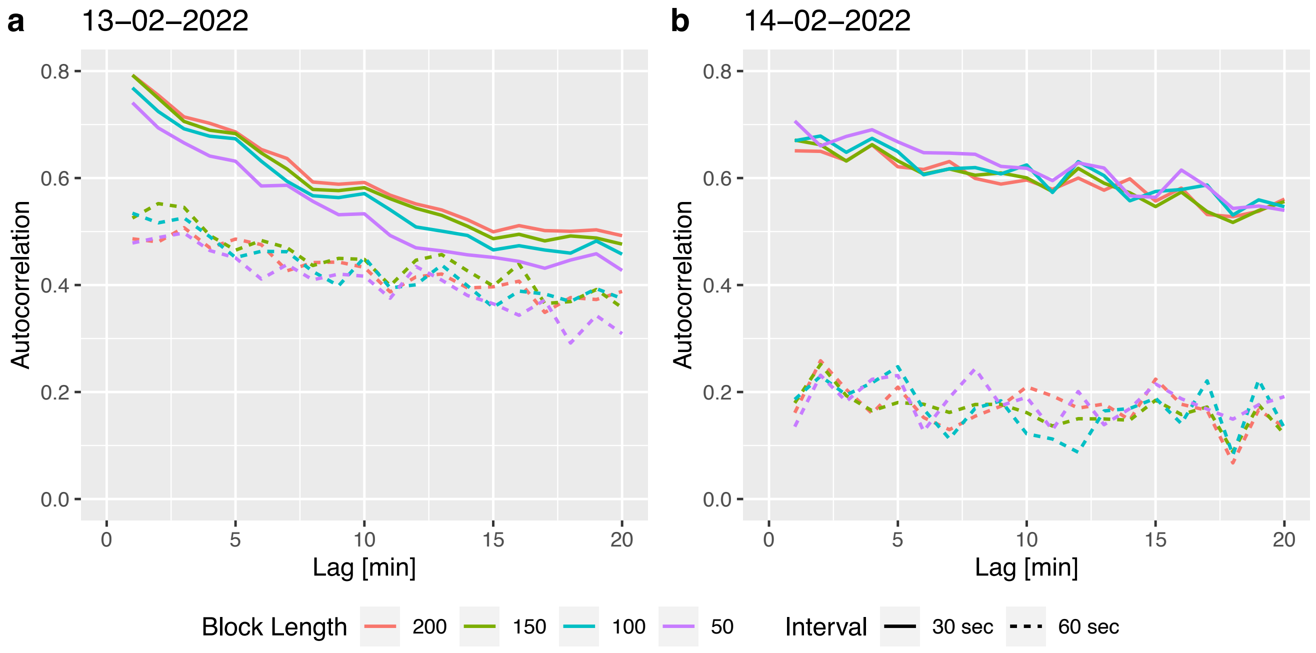

Figure 8. Autocorrelogram for U components for varying resolutions of the image with the same block region and the two frame intervals on February 13 and 14, 2022 shows the effect of the changing resolution and time intervals on the stability of the motion vectors.

interpreted as a quantitative validation of the algorithm, however, significant correlations of the magnitudes indicate that the estimates of the instantaneous CMVs from the camera images are stable over a long period.

To qualitatively compare the hourly mean CMV with winds of appropriate altitudes, we identified the hours with a stable CBH for at least 20 minutes from the ceilometer measurements from October 14, 2017, to August 14, 2019. The hourly winds are averaged for 1-km deep layers from the surface to 4 km altitude, and then the hourly-mean CMVs are compared with the mean wind vectors in the vertical layer corresponding to the median CBH (Fig. 9). From the 551 days of data during this period, 876 daytime cloudy hours were identified, when simultaneous measurements from the WPR, the ceilometer, and CMV estimates were available. We only present CMVs for one setting: the 40-pixel block length, and the 30-second frame interval for the red channel. The rainy samples, identified using the method described in section 2.4 mostly fall close to zero value, as no mean motion is recorded. The sky-view camera data routinely suffers from rain, snow, and other debris on the lens that obstructs the view. The higher wind speeds near zero CMV can mainly occur due to the snow obstructing the view, or smooth flat clouds bases that are not successfully tracked. In addition, the quality of the wind profiles from the WPR is also adversely affected by rainfall (Muradyan and Coulter, 2020). Therefore, we removed instances with precipitating events from consideration in our comparison. The correlation coefficient (r) of the U component of the CMV and hourly wind averages improved from 0.38 for all the data, to 0.42 after removing rainy samples, with a 95 % confidence interval. Likewise, for V component, r increased from 0.56 for all data to 0.59, with a 95 % confidence interval. The slope of the linear fit for U

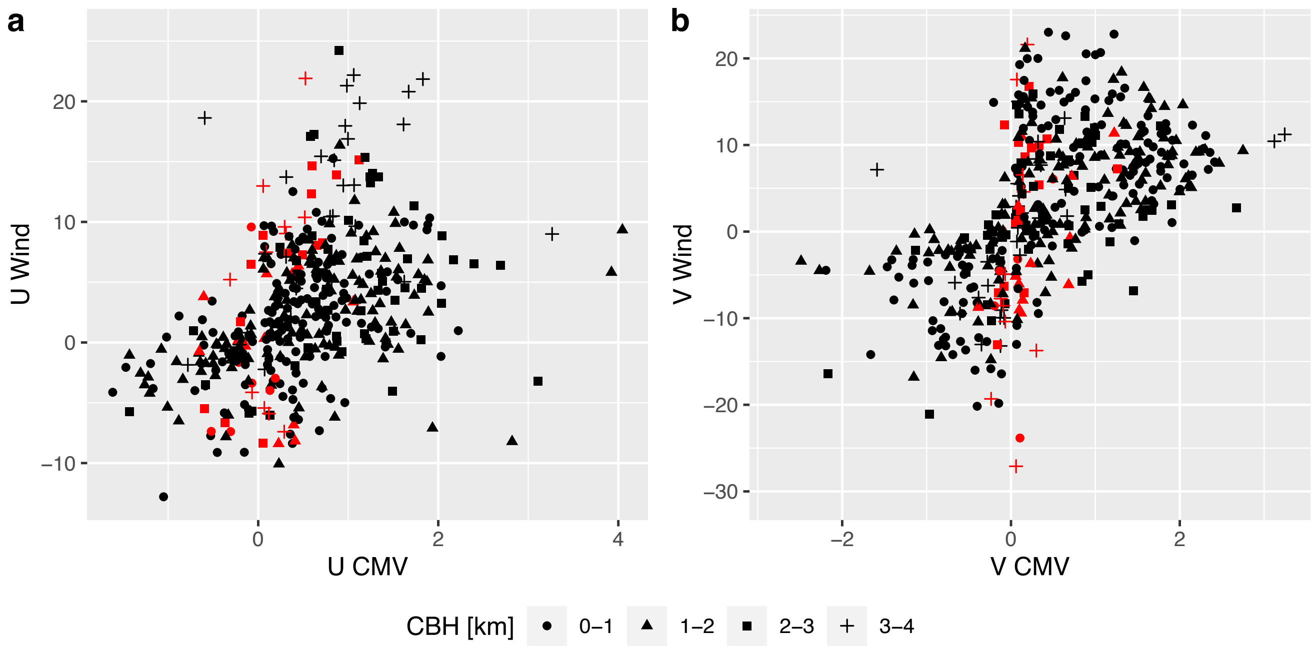

Figure 9. Comparison of hourly mean U and V components of the CMV and mean wind in a 1 km deep layer where the stable cloud base height was observed during the hour. The rainy hours extracted using the method in section 2.4 are shown with the red color.

components is between 2.4–3.4 for layers 0–3 km and it is 5.7 for the 3–4 km layer, suggesting that the mid-level (i.e. 3–4 km) CMVs are noticeably underestimated from the camera viewpoint. The slopes of the V components are in the range 3–4 for all layers. The WPR data above 4 km are sparse hence no samples with matching criteria were available during the study period.

4 Conclusion and Future Scope

Prior studies have documented the effectiveness of the block-wise phase correlation method for detecting cloud motion in IR and visible spectrum images (Leese et al., 1971; Dissawa et al., 2017; Zhen et al., 2019). We tested the sensitivity of the method to changes in block length, frame interval, image resolution, as well as five combinations of the visible channels from a sky-viewing camera. These results are also applicable for satellite and radar based motion estimation. Additionally, we compared the derived mean CMV with the observed mean wind field from a colocated remote sensing instrument, and presented a method to detect raindrops on the rotating dome.

The performance of different visible channels is comparable except for the red to blue channel ratio (RB). Although the RB is effective in segmenting clouds from the blue sky background, it smooths the cloud texture during overcast conditions, reducing the performance of the PC method. The red and grayscale performed slightly better than the blue and green channels.

We find that larger block sizes provide a more stable estimation of cloud motion, and the stability benefits largely from shortened interval between frames even for coarse resolution camera data. Considering that the temporal changes in cloud patterns reduce the quality of the motion vectors, a shorter frame interval helps in maintaining the structure from one image to the next. However, a larger block size allows for a larger sample for stable correlation matching, achieving more stable estimates of the motion during disorganized cloud conditions (Fig. 6 c and d). Although averaging in time over the short frame interval is a better way to achieve reliable estimates, a higher sampling rate may not be always feasible. In these situations, *the large block size that can capture homogeneous motion is recommended* for block-based PC implementation. We also show that increasing the spatial resolution, i.e. increasing the number of pixels without decreasing the number of blocks, marginally affects the quality of the motion vectors. At the same time, reducing the frame interval from 60 sec to 30 sec outperforms quadrupling of the resolution. Comparable results were obtained by Wang et al. (2018) for cloud segmentation using a ground-based camera.

Our analysis shows that doubling the frame rate outperforms quadrupling of the resolution. This non-intuitive result is very interesting in the context of edge-computing. Because a shorter frame interval between the camera images effectively improves the quality of the CMVs, it is important that the application has a deterministic and low-latency access to sky images. Edge-computing solves this problem efficiently by carefully placing and pairing computation with sensor data sources. Without incurring large data transfers and delays due to network outages, in an edge-computing platform like Sage, image data can be acquired and processed right next to the camera, in the field. The high-level motion estimation result which is much smaller and compresses efficiently, can be communicated and archived for further studies.

Current machine learning algorithms for automatic cloud identification underperform in the presence of thin clouds (Park et al., 2021). To this end, we are generating a dataset of thin clouds identified by scanning Mini Micropulse LIDAR (MiniMPL) and a co-located sky-viewing camera using edge-computing paradigm. One of the objectives is to use the camera images to predict cloud boundaries and the cloud motion, and utilize the knowledge to modify the MiniMPL settings to adapt scan strategies in real-time for optimal sampling in various environmental conditions.

Code availability. The Sage plugin implementation on the waggle platform is made available from https://portal.sagecontinuum.org/ and the full source code is available on Github at https://github.com/waggle-sensor/plugin-cmv-fftpc

.

Data availability. The data were obtained from the Atmospheric Radiation Measurement (ARM) user facility, a U.S. Department of Energy (DOE) Office of Science user facility managed by the Biological and Environmental Research Program. The ARM SGP data can be obtained from the following DOI 10.5439/1025309 (Total Sky Imager), 10.5439/1181954 (Ceilometer), and 10.5439/1025135 (Radar Wind Profiler). Sage camera data was collected at the Argonne Testbed for Multi-scale Atmospheric Observational Science (ATMOS). The ATMOS data used in this paper can be obtained by sending requests to the authors.

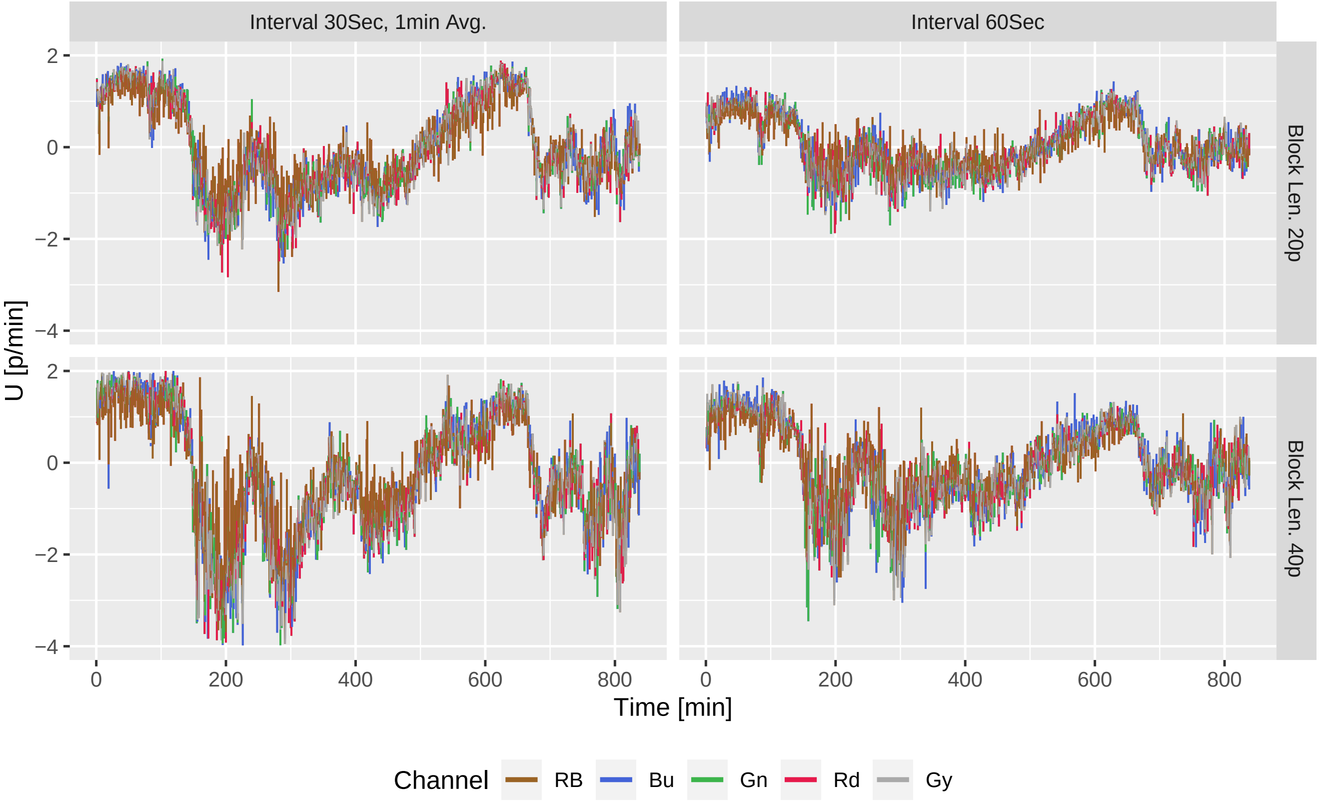

Figure A1. Unprocessed time series of U component of domain averaged CMV $[\text{pixel}\cdot\text{min}^{-1}]$ on 26 July 2016, 06:36 to 20:35 CDT (11:36-01:35 next day in UTC) over Lamont, OK. Variation with block size (20 pixels and 40 pixels) and frame intervals (30 sec and 60 sec) are shown for 5 channels. The smoothed data is shown in Fig. 3.

Appendix A: Raw CMV Output

255 The unprocessed 1-min time series of U and V components of CMV are shown in Fig. A1 and A2.

Author contributions. All authors contributed to the analysis plan and editing of the paper. BR designed the methodology and conducted sensitivity tests, data analysis, and plotting. SS, SP, and DD assisted in the algorithm selection and coding. SS, YK, and JS contributed to the development of the Sage plugin. RS, SP, NC, SS, and WG are responsible for the deployment, testing, and scheduling of the plugin on the waggle nodes for real-time use. BR, PM, and RJ lead the composition of the paper. PM contributed to the wind data analysis. SC, NF, PB conceptualized the work, provided project oversight, and direction. 260

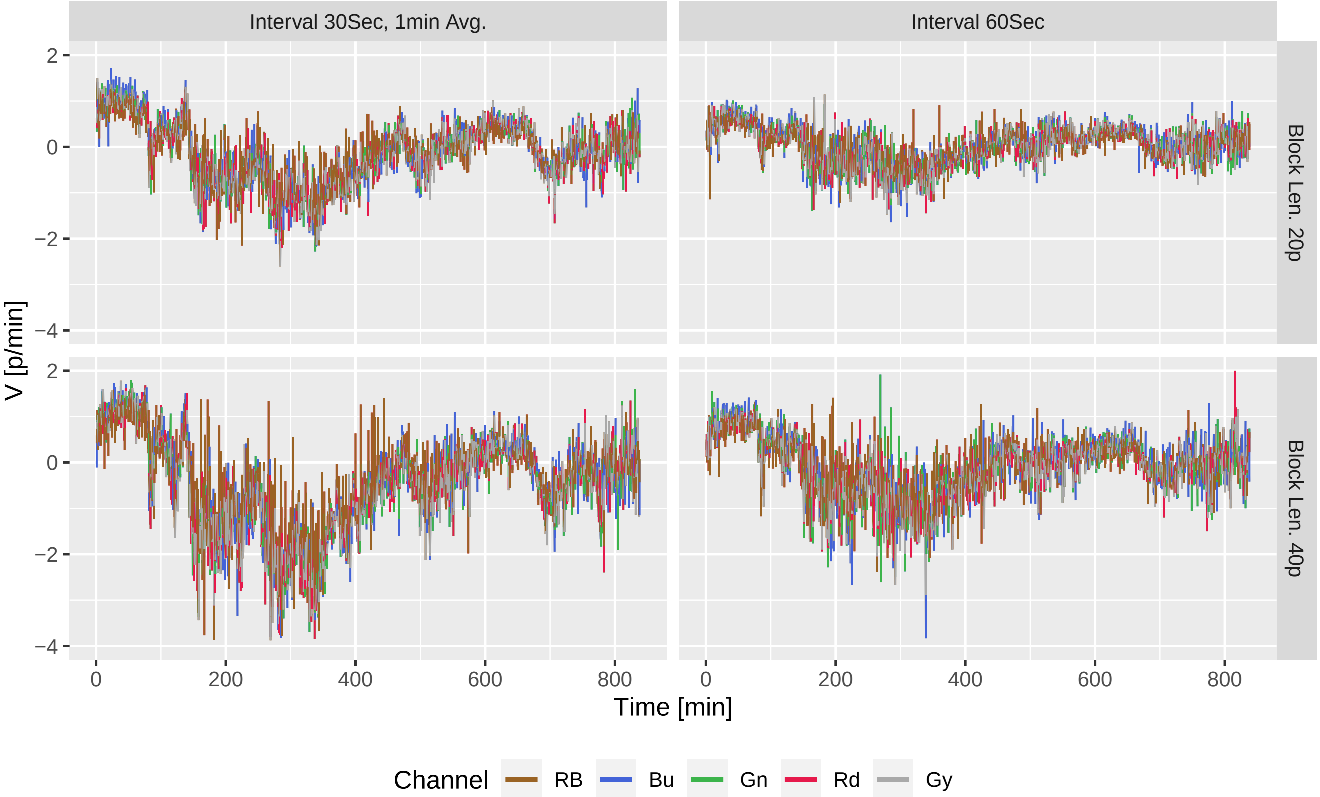

Figure A2. Same as Figure A1 but for V component of the CMV.

Competing interests. The authors declare that they have no conflict of interest.

Acknowledgements. The Sage project is funded through the U.S. National Science Foundation's Mid-Scale Research Infrastructure program, NSF-OAC-1935984. Argonne National Laboratory's contribution is based upon work supported by Laboratory Directed Research and Development (LDRD) funding from Argonne National Laboratory, provided by the Director, Office of Science, of the U.S. Department of Energy under Contract No. DE-AC02-06CH11357. We gratefully acknowledge the computing resources provided on Bebop, a high-performance computing cluster operated by the Laboratory Computing Resource Center at Argonne National Laboratory. We thank the ATMOS observatory staff for their assistance. The algorithm, data analysis, and graphics were programmed in Python (https://www.python.org/) and the R programming language (http://www.R-project.org).

References

Beckman, P., Sankaran, R., Catlett, C., Ferrier, N., Jacob, R., and Papka, M.: Waggle: An open sensor platform for edge computing, in: 2016 IEEE SENSORS, pp. 1–3, IEEE, 2016.

Chalasinska-Macukow, K., Turon, F., Yzuel, M., and Campos, J.: Contrast performance of pure phase correlation, Journal of optics, 24, 71, 1993.

Denman, S., Fookes, C., and Sridharan, S.: Improved simultaneous computation of motion detection and optical flow for object tracking, in: 2009 Digital Image Computing: Techniques and Applications, pp. 175–182, IEEE, 2009.

Dissawa, D., Godaliyadda, G., Ekanayake, M., Ekanayake, J. B., and Agalgaonkar, A. P.: Cross-correlation based cloud motion estimation for short-term solar irradiation predictions, in: 2017 IEEE International Conference on Industrial and Information Systems (ICIIS), pp. 1–6, IEEE, 2017.

El Jaouhari, Z., Zaz, Y., and Masmoudi, L.: Cloud tracking from whole-sky ground-based images, in: 2015 3rd International Renewable and Sustainable Energy Conference (IRSEC), pp. 1–5, IEEE, 2015.

Gacal, G. F. B., Antioquia, C., and Lagrosas, N.: Trends of night-time hourly cloud-cover values over Manila Observatory: ground-based remote-sensing observations using a digital camera for 13 months, International Journal of Remote Sensing, 39, 7628–7642, 2018.

Heinle, A., Macke, A., and Srivastav, A.: Automatic cloud classification of whole sky images, Atmospheric Measurement Techniques, 3, 557–567, 2010.

Huang, H., Yoo, S., Yu, D., Huang, D., and Qin, H.: Cloud motion detection for short term solar power prediction, in: ICML 2011 Workshop on Machine Learning for Global Challenges, 2011.

Jiang, J., Lv, Q., and Gao, X.: The ultra-short-term forecasting of global horizonal irradiance based on total sky images, Remote Sensing, 12, 3671, 2020.

Kazantzidis, A., Tzoumanikas, P., Bais, A. F., Fotopoulos, S., and Economou, G.: Cloud detection and classification with the use of whole-sky ground-based images, Atmospheric Research, 113, 80–88, 2012.

Leese, J. A., Novak, C. S., and Clark, B. B.: An automated technique for obtaining cloud motion from geosynchronous satellite data using cross correlation, J. Appl. Meteor., 10, 118–132, 1971.

Morris, V.: ARM: Total Sky Imager (TSI): fractional sky coverage, https://doi.org/10.5439/1025308, 2000.

Morris, V.: Total Sky Imager (TSI) Handbook, Atmospheric Radiation Measurement Rep. ARM TR-017, https://doi.org/10.2172/1020716, 2005.

Morris, V., Zhang, D., and Ermold, B.: ceil, https://doi.org/10.5439/1181954, 1996.

Morris, V. R.: Ceilometer Instrument Handbook, https://doi.org/10.2172/1036530, 2016.

Muradyan, P. and Coulter, R.: ARM: 915-MHz Radar Wind Profiler/RASS (RWP915): wind consensus data, https://doi.org/10.5439/1025135, 1998.

Muradyan, P. and Coulter, R.: Radar Wind Profiler (RWP) and Radio Acoustic Sounding System (RASS) Instrument Handbook, https://doi.org/10.2172/1020560, 2020.

Park, S., Kim, Y., Ferrier, N. J., Collis, S. M., Sankaran, R., and Beckman, P. H.: Prediction of Solar Irradiance and Photovoltaic Solar Energy Product Based on Cloud Coverage Estimation Using Machine Learning Methods, Atmosphere, 12, 395, 2021.

Raut, B. A., Karekar, R. N., and Puranik, D. M.: Wavelet-based technique to extract convective clouds from infrared satellite images, IEEE Geosci. Remote Sens. Lett., 5, 328–330, 2008.

Raut, B. A., Jackson, R., Picel, M., Collis, S. M., Bergemann, M., and Jakob, C.: An Adaptive Tracking Algorithm for Convection in Simulated and Remote Sensing Data, J Appl Meteorol Clim, 60, 513–526, https://doi.org/10.1175/jamc-d-20-0119.1, 2021.

Slater, D., Long, C., and Tooman, T.: Total sky imager/whole sky imager cloud fraction comparison, in: Proc. 11th ARM Science Team Meeting, pp. 1–11, 2001.

Steiner, M., Houze Jr, R. A., and Yuter, S. E.: Climatological characterization of three-dimensional storm structure from operational radar and rain gauge data, J. Appl. Meteor., 34, 1978–2007, 1995.

Turon, F., Chalasinska-Macukow, K., Campos, J., and Yzuel, M. J.: Pure phase correlation applied to multi-object colour scenes, Journal of optics, 28, 112, 1997.

Voronych, O., Höller, R., Longhi Beck, G., and Traunmüller, W.: Solar PV nowcasting based on skycamera observations, Advances in Science and Research, 16, 7–10, 2019.

Wang, Y., Wang, C., Shi, C., and Xiao, B.: A selection criterion for the optimal resolution of ground-based remote sensing cloud images for cloud classification, IEEE Transactions on Geoscience and Remote Sensing, 57, 1358–1367, 2018.

Westerweel, J. and Scarano, F.: Universal outlier detection for PIV data, Experiments in fluids, 39, 1096–1100, 2005.

Wood-Bradley, P., Zapata, J., Pye, J., et al.: Cloud tracking with optical flow for short-term solar forecasting, in: Proceedings of the 50th Conference of the Australian Solar Energy Society, Melbourne, Citeseer, 2012.

Zhen, Z., Xuan, Z., Wang, F., Sun, R., Duić, N., and Jin, T.: Image phase shift invariance based multi-transform-fusion method for cloud motion displacement calculation using sky images, Energy Conversion and Management, 197, 111 853, 2019.